JOURNAL OF AIRCRAFT
Vol. 42, No. 4, July–August 2005

Numerical Simulations of Membrane Wing Aerodynamics for Micro Air Vehicle Applications

Yongsheng Lian* and Wei Shyy†
University of Florida, Gainesville, Florida 32611-6250

To gain insight into the aerodynamics of flexible wing-based micro air vehicles (MAVs), we study the three-dimensional interaction between a membrane wing and its surrounding fluid flow. A nonlinear membrane structural solver and a Navier–Stokes flow solver are coupled through the moving boundary technique and time synchronization. Under the chord Reynolds number of 9×10^4, the membrane exhibits self-initiated vibrations in accordance with its material properties and the surrounding fluid flow. The vertical flow structure, its effect on the aerodynamic parameters, and the implications of the membrane deformation on the effective angle of attack and flow structure are discussed.

Nomenclature

C_D = drag coefficient
C_L = lift coefficient
c = chord length
c_p = pressure coefficient
D = drag
F_{px} = form drag
F_{py} = lift caused by pressure force
$F_{\tau\mathrm{x}}$ = drag caused by friction
L = lift
U = freestream speed
u = chordwise velocity
v = vertical velocity
x = chordwise distance from the leading edge
Z = half-wing span
z = spanwise distance from the root
α = angle of attack

I. Introduction

MICRO air vehicles (MAVs) with a maximal dimension of 15 cm and a flying speed of around 10 m/s are of interest to both military and civilian applications. For example, they can be used for battlefield surveillance or mapping the extent of chemical/radiation spills. Equally useful civil applications include search and rescue operations, traffic and news coverage, and environmental monitoring.[1,2] As MAVs reduce in size, they can operate with lower stalling speeds,[1] defined as the minimum speed at which sufficient lift is produced for flight. However, the correspondingly low Reynolds number degrades the aerodynamic performance, such as the lift-to-drag ratio. Furthermore, the vehicle becomes more sensitive to the wind effect, considering the wind speed can often be comparable to the flight speed. It has been demonstrated that flexible membrane wings are appropriate for the MAVs[1] because they can adapt their shapes in response to the flight environment, and the stalling margin can be extended because of such a passive control capability.[3]

Unlike a rigid wing, a membrane wing exhibits self-initiated unsteady response even in a steady-state freestream.[3,4] Such response and associated shape changes affect the wing aerodynamics, which in turn affect the membrane dynamics, resulting in a fluid- and-structure interaction problem.

To date, the study of membrane and fluid flow interactions is limited. Jackson and Christie[5] adopted a three-dimensional potential flow-based solver and a membrane wing model to analyze the aeroelastic behavior of marine sails. Smith and Shyy[6] and Shyy et al.[7] presented a computational approach to model the interaction between a two-dimensional flexible membrane wing and surrounding viscous flows. All of these works use static linear membrane models. Lian et al.[4] proposed a nonlinear dynamic membrane model to study the interaction between a three-dimensional membrane wing and viscous fluid flow. In that work, external forces are obtained by solving the Reynolds-averaged Navier–Stokes equations with k–ϵ turbulence model.[8] In the present effort, we have further improved computational capability by adopting a more efficient time-marching flow solver. We have also extended the fluid-and-structure computations to cases involving different angles of attack, and we have obtained solutions for both membrane and rigid wings for a direct assessment.

In the present work we first evaluate the rigid-wing performance for comparative purposes, focusing on the aerodynamic characteristics associated with the low-aspect-ratio and low-Reynolds-number wing, such as tip vortices, leading-edge separation, and the resulting unsteady phenomenon. Next we investigate computational techniques for the membrane wing in regard to the issues associated with the fluid-and-structure interaction, such as time synchronization and the geometric conservation law.[9] The pressure distributions, membrane wing deformations, resulting effective angles of attack of the membrane wing, and aerodynamic coefficients are assessed in comparison to those of the rigid wing.

II. Governing Equations and Computational Techniques

The solution method described here is based on the work of Lian et al.,[4,10] in which a finite element formulation for large strain plane-stress problems is proposed to deal with the structural deformation. The full Navier–Stokes equations in curvilinear coordinates are adopted to compute the fluid flow and aerodynamic forces. A moving grid technique is employed to automatically regenerate the new computational-fluid-dynamics (CFD) grid after the shape change. The thin-plate interpolation method[11] is used as the interface to exchange information between the fluid solver and the structural solver. Subiteration between the fluid solver and structural solver at each time step is enforced to control the error caused by phase lag.

Presented as Paper 2003-1726 at the AIAA/ASME/ASCE/AHS 44th Structures, Structural Dynamics, and Materials Conference, Norfolk, VA, 7–10 April 2003; received 19 October 2003; revision received 15 January 2004; accepted for publication 16 January 2004.

*Ph.D., P.O. Box 116250, Department of Mechanical and Aerospace Engineering; currently Visiting Scholar, Department of Aerospace Engineering, University of Michigan, Ann Arbor, MI, 48109. Member AIAA.

†Professor and Chair, P.O. Box 116250, Department of Mechanical and Aerospace Engineering. Fellow AIAA.

Below we give a short description of each specific computational feature.

The membrane material is assumed to obey the hyperelastic Moody–Rivlin model, for which the strain energy function W can be written as

$$W = c_1(I_1 - 3) + c_2(I_2 - 3) \tag{1}$$

where I_1 and I_2 are the first and second invariants of the Green deformation tensor and c_1 and c_2 are two material property parameters. The Moody–Rivlin model is one of the most frequently employed hyperelastic models because of its mathematical simplicity and good accuracy for relatively large strains (less than 150%).[12]

The finite element procedure is based on the principle of virtual work. We use a first-order triangular element to discretize the spatial domain. Because the structural solver is computationally much cheaper than the fluid solver, we can achieve the desired resolution by refining the structural mesh. The dynamic membrane response under the external force is described by the following equation:

$$\boldsymbol{M}\ddot{\boldsymbol{D}}(t) + \boldsymbol{F}^{\text{int}} = \boldsymbol{F}^{\text{ext}} \tag{2}$$

where $\boldsymbol{M}$ is a positive-definite mass matrix, which remains constant during the computation; $\boldsymbol{D}(t)$ represents the displacement vector; $\ddot{\boldsymbol{D}}(t)$ is the acceleration vector; $\boldsymbol{F}^{\text{int}}$ is the internal force caused by the shape change, and $\boldsymbol{F}^{\text{ext}}$ is the generalized external force. To integrate Eq. 2, we use the implicit Wilson-θ method,[13] which is second-order accurate for linear systems of equations. Our numerical tests show that the overall accuracy for the membrane model is approximately first order.[4]

The fluid solver is based on the full Navier–Stokes equations for the incompressible fluid flow in curvilinear coordinates.[8] A pressure-based algorithm based on the pressure-implicit with splitting of operators (PISO) method[14] is utilized. The PISO method is a predictor-corrector technique treating the velocity and pressure field with successive updates. In general, the PISO method is more efficient for transient flow computations.[14] We use the second-order upwind scheme[8] for the convection terms, and all of the other spatial derivative terms are discretized with the second-order central difference schemes. In all of our computations, a converged solution is obtained once the residuals decrease by an order of three.

One important issue involved in the fluid-and-structure interaction problem is how to regenerate the CFD grid after the shape change. Several approaches have been proposed for this purpose. In our approach, we use the perturbation method to regenerate the grid.[15,16] A main feature of this method is that it can preserve the good quality of the original grid. For a one-dimensional problem, it simply follows the formula

$$x_i^{\text{new}} = x_i^{\text{old}} + S_i^{\text{old}}\left(x_s^{\text{new}} - x_s^{\text{old}}\right) \tag{3}$$

where x_i represents the location of interior grid point, x_s is the location of grid point on a boundary, and S is the normalized arc length along the radial mesh line measured from the outer domain. Specifically,

$$S_i = \frac{\sum_{l=1}^{i}\sqrt{(x_{l+1}-x_l)^2 + (y_{l+1}-y_l)^2 + (z_{l+1}-z_l)^2}}{\sum_{l=1}^{n}\sqrt{(x_{l+1}-x_l)^2 + (y_{l+1}-y_l)^2 + (z_{l+1}-z_l)^2}} \tag{4}$$

We exchange information between the fluid and structural solvers by interpolation and extrapolation. We adopt the thin-plate-spline (TPS) method by Duchon[11] because it is a global interpolation suitable for the interpolation between the structured CFD grid and the unstructured computational-structure-dynamics (CSD) grid. The TPS method also uses smooth interpolation function, which has a continuous first-order derivative.

III. Results and Discussion

A. Membrane-Wing Definition

Figure 1a shows the 15-cm MAV with a flexible wing designed by Ifju and coworkers.[17] The membrane wing consists of a leading-edge spar and three chordwise battens made of unidirectional carbon-fiber prepreg laminate. A membrane material is bonded to the spar and battens. The membrane wing has a span of 15.2 cm, a root chord of 13.7 cm, a mean chord of 10.5 cm, wing area of 160 cm^2, and a low aspect ratio of 1.44. The wing camber is approximately of 6% of the chord at the root and decreases to 2% at the tip. In this configuration, the maximum camber is located at 27% chord at the root. Based on the freestream velocity of 10 m/s, the root-chord Reynolds number is 9×10^4.

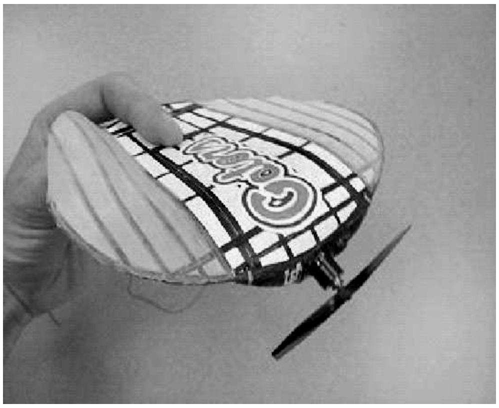

a) 15 cm MAV with membrane wing

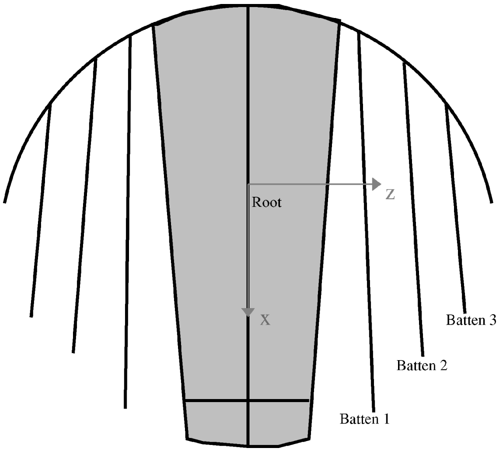

b) Schematic wing with three battens

Fig. 1 15 cm MAV with member wing.

Instead of considering the whole vehicle, in this work we focus on the wing without the fuselage and propellers. To save computational time, only half-wing is considered. A schematic geometry of the wing is shown in Fig. 1b. The shaded area corresponds to the fuselage, which does not change the shape. As discussed before, the membrane wing consists of two materials with different properties: the membrane is flexible, which does not sustain bending moment; the carbon fiber is rigid, which provides support for the membrane and can sustain bending moment. To fully model the membrane wing, a model needs to account for both the rigid battens and the flexible membrane. Two main difficulties arise by doing that. First, because the membrane does not sustain bending moment, it has three degrees of freedom at each node; the batten, if modeled as a beam, has six degrees of freedom at each node. Special treatments are required to handle the interface point, which belongs to different regimes and has different degrees of freedom. Second, the membrane is much thinner than the batten, and hence the assembled mass matrix will be very ill conditioned. Given these factors, we treat the batten as a special membrane material with larger density; the density ratio between the batten and the membrane is three.

B. Rigid-Wing Dynamics

A grid sensitivity test is done on the half-rigid wing by Lian et al.[4] We tabulate the results in Table 1. Three grid systems have been systematically chosen, ranging from 1.8×10^5 points at the coarse level and 2.3×10^6 points at the fine level on the half-wing. Under such a low-Reynolds-number condition, true grid-independent results are difficult to attain. Given the available computing resource and the aforementioned investigation, we use the intermediate grid, which has 6.7×10^5 points for the rigid-wing simulation, and use the coarse grid to illustrate the key issues in the fluid and flexible structure interaction problems. Our purpose is to demonstrate the salient features of membrane-wing computations and the related aerodynamic and structural characteristics.

Tip vortices exist on a finite wing as a result of the pressure difference between upper and lower wing surfaces. In general, the tip vortex effects are two-fold:

1) The tip vortex causes downwash, which decreases the effective angle of attack and increases the drag.[18]

Table 1 Grid refinement study on the half-rigid wing

Grid ($NX \times NY \times NZ$)	Grid on the wing surface	F_{px}	F_{py}	$F_{\tau\text{x}}$	L/D[a]
Coarse $83 \times 42 \times 52$	41×31	$3.12E-2$	$2.55E-1$	$4.85E-3$	7.06
Intermediate $123 \times 62 \times 72$	61×41	$3.08E-2$	$2.54E-1$	$4.61E-3$	7.16
Fine $183 \times 122 \times 102$	101×61	$3.10E-2$	$2.52E-1$	$4.40E-3$	7.10

[a] L/D = lift-to-drag ratio.

2) The tip vortex forms a low-pressure region on the top surface of the wing, which provides additional lift.[19]

For the present low-aspect-ratio wing, it is important to investigate the tip-vortex effects on the wing aerodynamics. Figure. 2 visualizes the evolution of the vortical structure with the increase of angle of attack. The pressure distributions on the upper surface are also presented. At $\alpha = 6$ deg, tip vortices are clearly visible even though they only cover a small area and are of modest strength. The flow is attached to the upper surface and follows the chordwise direction. A low-pressure region near the tip is observed, which is caused by the tip vortex. This pressure drop can also be seen from Fig. 3a, where the spanwise pressure coefficients at different angles of attack at $x/c = 0.4$ are plotted. At $\alpha = 6$ deg the spanwise pressure is essentially uniform on the upper surface, and the tip vortex causes the pressure drop to occur at approximately 90% of the span from the root. Figure. 3 is illustrative in regard to the salient features of pressure vs vortical structures. They are not indicative of the total level of the pressure force.

Vortices strengthen with an increase in angle of attack. At $\alpha = 27$ deg, as shown in Fig. 2, tip vortices develop a strong swirl motion while entrain the surrounding flow. In Fig. 2f we also show the pressure contour at $\alpha = 39$ deg. The pressure drop further strengthens the swirl by attracting more fluids toward the vortex core, which in turn decreases the pressure in the vortex core.

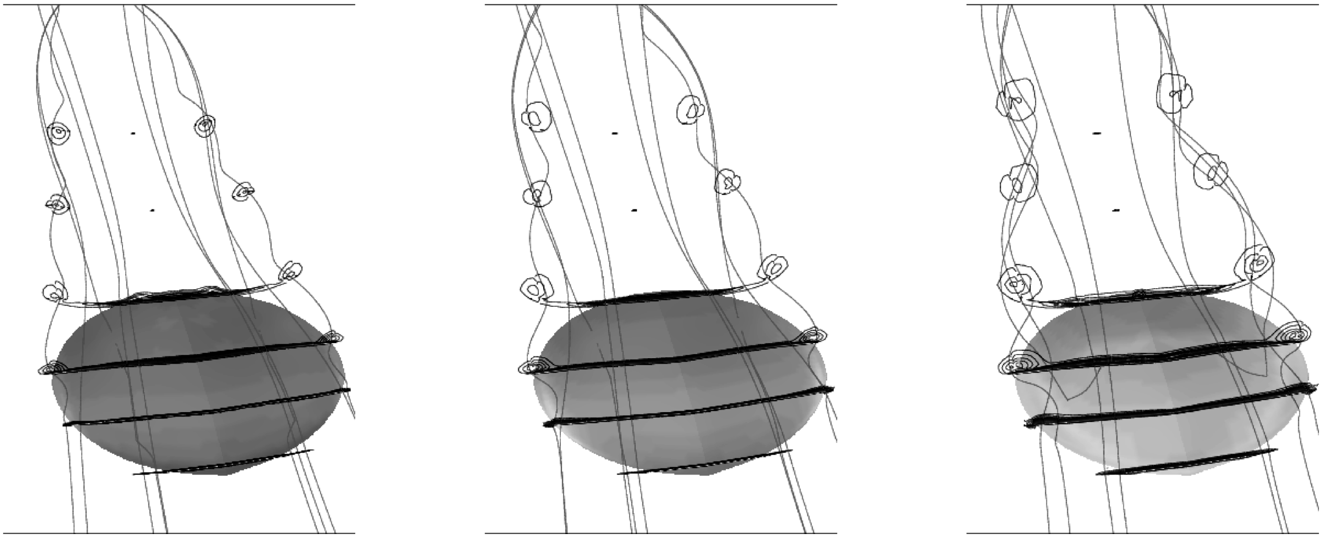

a) $\alpha = 6$ deg **b) $\alpha = 15$ deg** **c) $\alpha = 27$ deg**

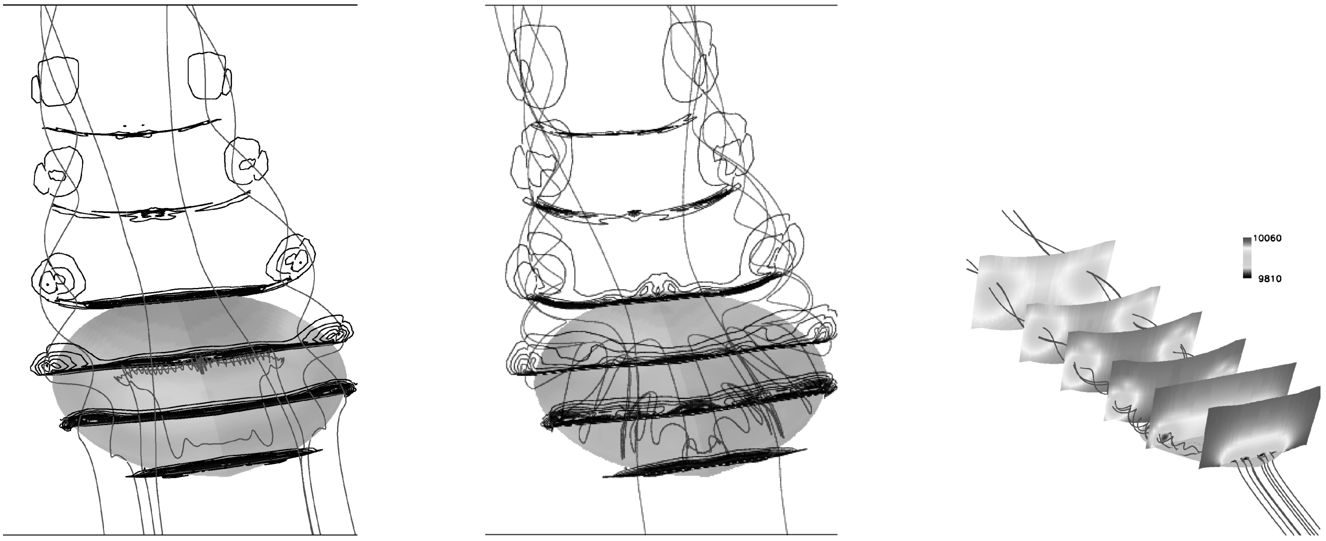

d) $\alpha = 39$ deg **e) $\alpha = 51$ deg** **f) Pressure contours at $\alpha = 39$ deg**

Fig. 2 Streamlines and vortices for rigid wing at different angles of attack.

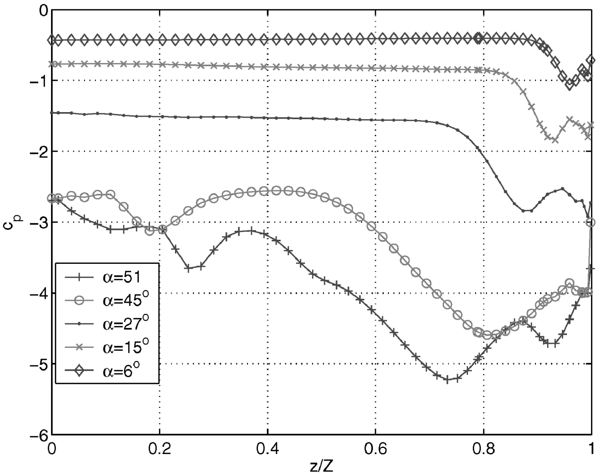

a) c_p **at upper surface**

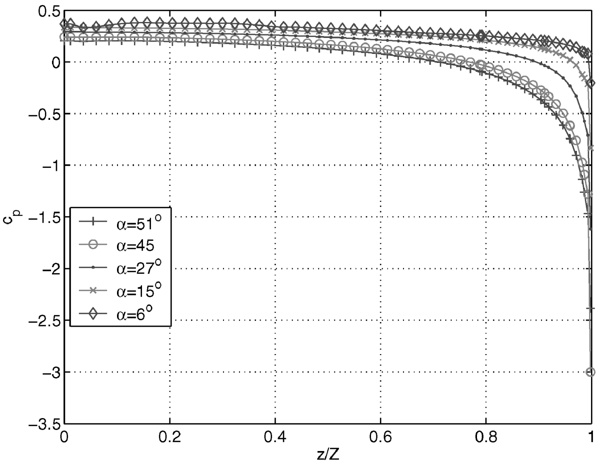

b) c_P **at lower surface**

Fig. 3 Spanwise pressure coefficient distributions at $x/c = 0.4$ **for rigid wing at different angles of attack.**

Toward downstream, the pressure recovers to its ambient value, the swirling weakens, the diameter of the vortex core increases, and the vortex core loses its coherent structure.

The low-pressure area increases with the increase in angle of attack. In Fig. 3a, the pressure drop moves towards the root and now occurs at 75% from the root. At lower angle of attack, the vortex core position, which corresponds to the nadir in Fig. 3a, shows a linear relation to the angle of attack. This relation disappears at higher angles of attack when flow is separated from the upper surface. For example, at $\alpha = 45$ deg, the flow is separated at the leading edge, and the low-pressure zone covers more than 40% of the wing surface, which helps to maintain the increase of lift. At $\alpha = 51$ deg, considerable spanwise velocity component is seen, and flow is separated from most of the upper surface (Fig. 2).

Tip vortices also have impacts on the lower surface-pressure distribution; however, the affected regions are mainly close to the tips. Most regions in the lower surface are not affected by the tip vortices. From Fig. 3b we can see the pressure distributions are almost uniform in spanwise direction even at high angles of attack. In addition to the force consideration, the moment is the other critical factor. Figure 3 indicates that the moment experiences substantial variations as the angle of attack changes.

The laminar boundary layer is prone to separate under an adverse pressure gradient. The separation is usually followed by a quick transition from laminar to turbulent flow. If the adverse pressure gradient is not too strong, the resulting turbulent flow, by obtaining energy through entrainment, can reattach to the surface and form an attached turbulent boundary layer.[20]

Based on the solutions obtained, we illustrate the bubble structures for different angles of attack in Fig. 4. Instantaneous plots of streamlines at the root section of the rigid wing are shown. At this moment, we exclude the spanwise velocity component to make a clear representation of these separated structures. At a lower angle of attack of 6 deg, the flow primarily attaches to the surface, and a tiny separation bubble is observed at the lower surface near the leading edge. Beginning at 45% chord from the leading edge, a weak recirculation zone is seen on the upper surface, which produces a reattachment length of $x/c = 0.5$. The maximum reverse velocity is less than 0.5% of the freestream velocity.

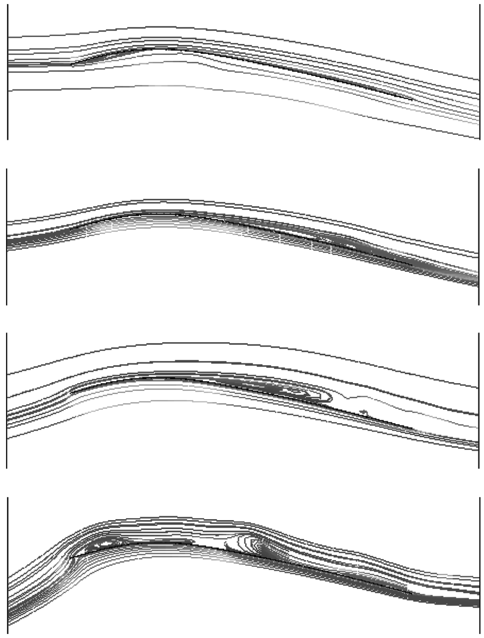

Fig. 4 Streamlines at different angles of attack for rigid wing. From top to bottom 6, 15, 27, and 51 deg. Shown are shots of the individual time-dependent flows.

With the increase of incidence, the separation point moves forward toward the leading edge; by gaining energy from the shear layer the maximal reverse velocity becomes larger. At the angle of attack of 15 deg, as shown in Fig. 4, flow separation occurs at 39% of chord from the leading edge. The shear-layer reattachment happens at 89% of the chord, which corresponds to a rapid increase in the surface pressure.

At $\alpha = 27$ deg, the strong reverse flow component of the separation bubble reaches a maximum mean velocity of $0.49U$. Under such a situation, Crompton and Barrett[21] have shown that the shear layer is particularly energetic because most of the shear layer is turbulent. Even though the flow on the upper surface near the root has separated from a large portion of the surface, the lift still increases with the angle of attack. Two observations can be made. First, tip vortices generate suction near the tip area (Fig. 3), which provides additional lift. Second, even though flow separates near the root, it still attaches to the surface in the other region. When the angle of attack increases further, at $\alpha = 51$ deg, massive separation occurs on most of the upper surface, and stall occurs.

Vortex shedding and boundary-layer separation usually introduce unsteadiness to the aerodynamic performance. Cummings et al.[22] have reported that at large angle of attack the computation under unsteady assumption predicts a much lower lift coefficient than that of the computation under steady assumption. In the present work, we perform computations under the steady assumption when the incidence is less than 15 deg while conducting computations under both steady and unsteady assumptions when the angle of attack is larger than 15 deg. It is observed that over a wide range of angles of attack the difference between the steady-state computations and the time-averaged unsteady computations are small even at large angle of attack in which unsteady phenomenon such as vortex shedding are prominent. The differences in lift coefficient and lift-to-drag ratio are found to be less than 1%. Figure. 5a compares the result between steady and unsteady computations. Visible differences appear only

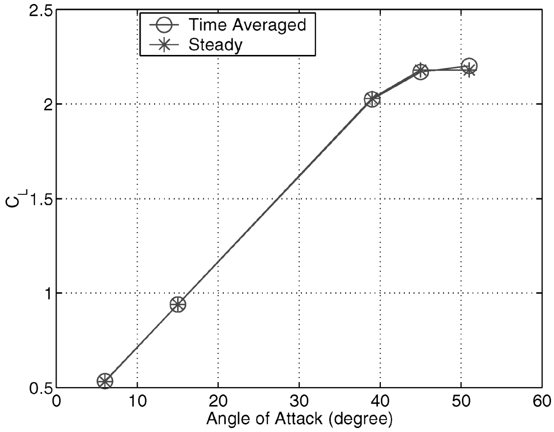

a) Computational results

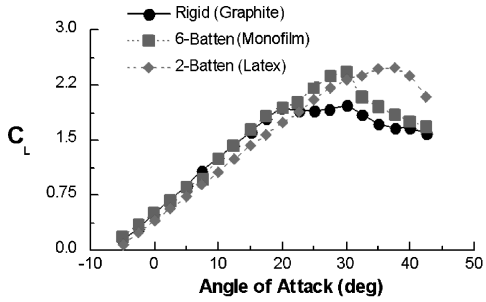

b) Experimental results[3]

Fig. 5 Comparison of rigid wing C_L for steady and unsteady computations.

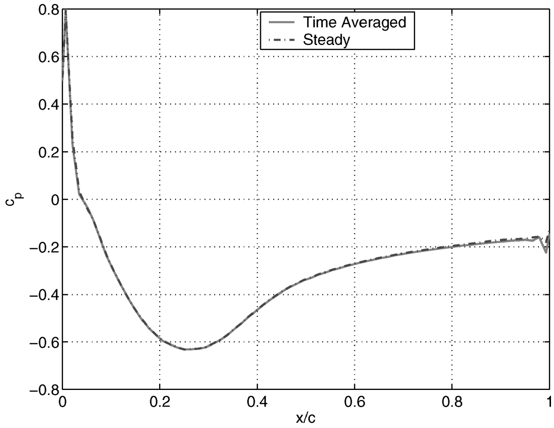

a) α = 6 deg

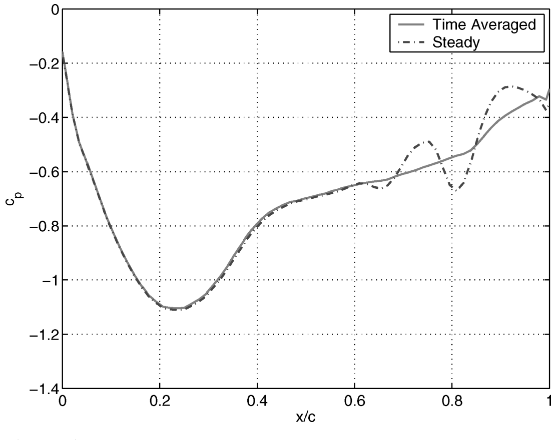

b) α = 15 deg

Fig. 6 Comparisons of c_p on rigid wing at the root for steady and unsteady computations.

at $\alpha = 51$ deg and beyond. In our computations, the lift-curve slope is approximately 2.44 for the rigid wing. Waszak et al.[3] have done experiments on a similar rigid wing with a Reynolds number and aspect ratio of 7×10^4 and 2.0, respectively. Their lift-curve slope, as shown in Fig. 5b, is approximately 2.9. It is understandable that our wing has a lower lift curve because of the lower aspect ratio of 1.44. than that used by Waszak et al.

We further compare the pressure distribution at the root section, where separation usually appears first as a result of the large camber in the present MAV wing design.[17] Figure 6 shows that at $\alpha = 6$ deg the time-averaged pressure coefficient matches closely with the steady-state result. This finding is consistent with the results shown in Fig. 4, where a very weak recirculation is seen at this angle of attack. However, at $\alpha = 15$ deg, clear difference is shown after $x/c = 0.6$, which approximately corresponds to the location of the maximal reverse velocity. The time-averaged value yields a smooth pressure distribution; the variation in the steady result appears to result from the recirculation zone. The difference between the steady and unsteady computations is also shown from the velocity distribution. At $\alpha = 6$ deg, as seen from Fig. 7a, there is almost no difference in the chordwise velocity distribution. At $\alpha = 15$ deg, difference is clearly seen at $x/c = 0.80$, which occurs after the separation bubble (see Fig. 7b).

C. Membrane-Wing Dynamics

In the present case, the membrane has a uniform thickness of 0.2 mm and a density of 1200 kg/m^3. We assign the battens with a higher density. The density ratio between batten and membrane is 3. The two parameters governing the membrane property shown in Eq. (2) take the values of $c_1 = 5.0 \times 10^5$ pa and $c_2 = 0.785c_1$. The

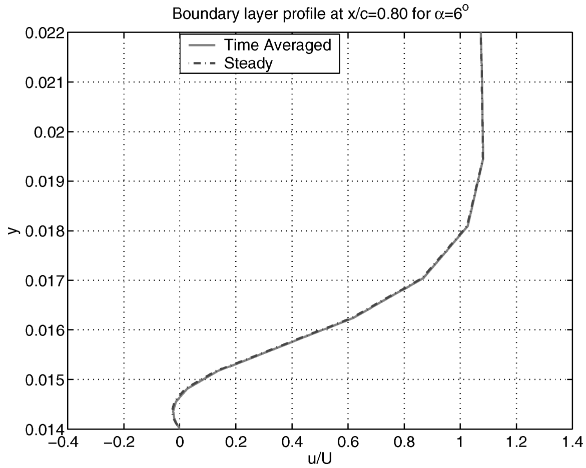

a) α = 6 deg

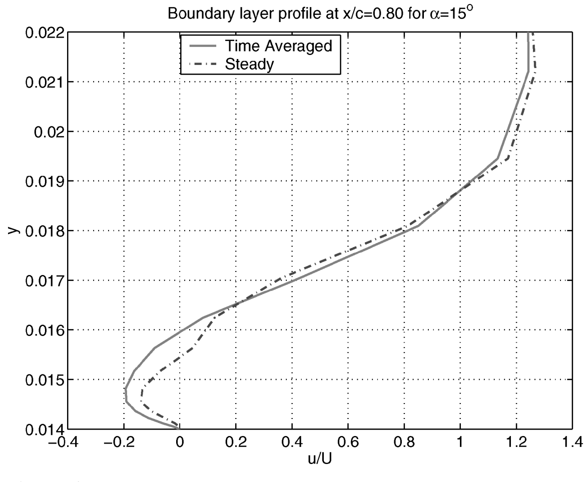

b) α = 15 deg

Fig. 7 Comparisons of chordwise velocity profiles on rigid wing for steady and time-averaged unsteady computations at the root location.

CSD grid employs 1030 nodes and 1938 triangular elements on the half-wing surface. For the structural solver, we choose $\theta = 1.4$ in the Wilson-θ scheme, and double-precision computation is applied to ensure the accuracy.

Each solver functions independently with its own computational grid and time step; the coupling is accomplished by exchanging information through an interface. The use of subiteration between the CFD solver and the CSD solver during each time step allows for the synchronization of the fluid and structure coupling and improves the overall accuracy. Figure 8a demonstrates the displacement history of a trailing-edge node. The computation without synchronization fails to continue. The displacement history without synchronization matches well with the synchronization at the very early stage. However, the lagging errors accumulate in time and eventually result in much larger displacement than that with synchronization. Gordnier and Visbal[23] also reported the importance of such a subiteration procedure. The velocity and pressure histories of the same node are shown in Figs. 8b and 8c, respectively. Before divergence occurs, the velocity computed without synchronization is more than two times higher than that with synchronization. The high velocity is apparently associated with the sudden pressure drop shown in Fig. 8c, which causes the wrinkle of the membrane and the blowout of the structural solver.

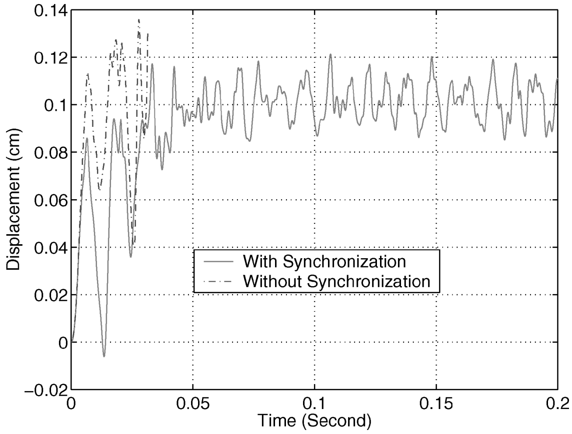

a) Displacement of a trailing-edge point

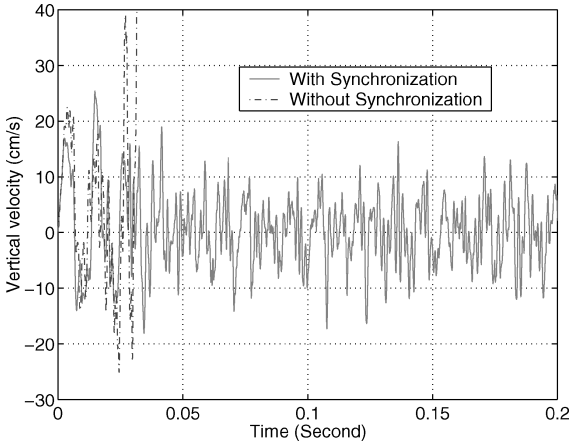

b) Vertical velocity of a trailing-edge point

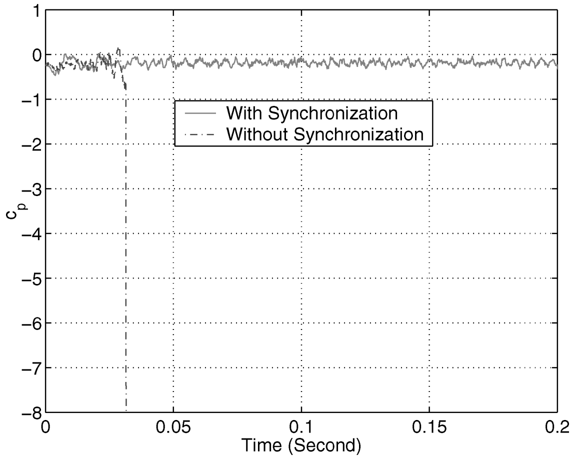

c) c_p on a trailing-edge point

Fig. 8 Effects of time synchronization for membrane wing at $\alpha = 6$ deg.

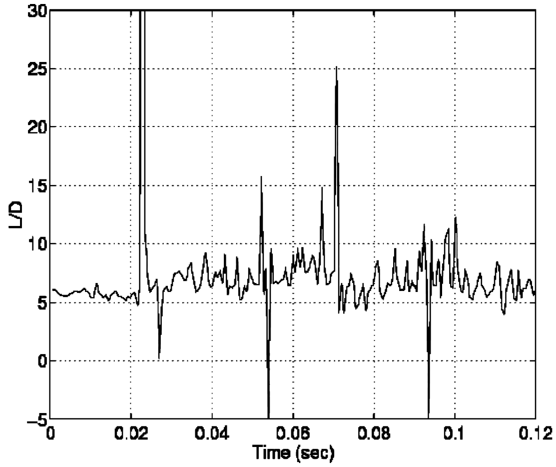

a) Not satisfying the geometric conservation law

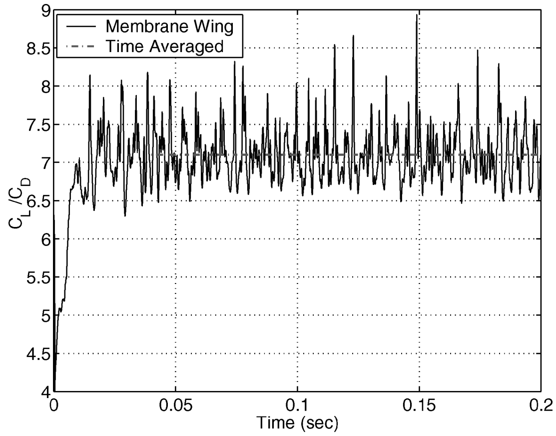

b) Satisfying the geometric conservation law

Fig. 9 Effect of the geometric conservation law on C_L/C_D for membrane wing computation at $\alpha = 6$ deg.

The geometric conservation law[9] is critical when the moving boundary problem is solved on body-fitting curvilinear coordinates. Figure 9a shows the time history of C_L/C_D for the membrane wing at $\alpha = 6$ deg. Without satisfying the geometric conservation law, irregular spikes are observed in the course of computation. However, the computations are better regulated once the geometric conservation law is enforced as in Fig. 9b. Farhat et al.[24] argued that the geometric conservation law is a necessary condition to maintain the stability of a scheme utilized in moving boundary problems. We do not come across instability issues in the present study. Nevertheless, the computations behave erratically when the geometric conservation law is not enforced.

Figure 10 demonstrates the displacement history of the trailing edge with time. The maximal displacement during that period occurs near the tip. The displacement is normalized by the maximal camber which is about 0.9 cm. There is no movement near the root because it is rigid. To investigate the vibration frequency, a Fourier analysis is performed on one point between the batten 1 and batten 2 on the trailing edge. Its displacement history is shown in Fig. 8a, and the dominated frequency is around 120 Hz (Fig. 11). Analyses at other

Table 2 Aerodynamic coefficients comparison between membrane wing and rigid wing

Head	Head	Membrane wing	Rigid wing
6 deg	C_L/C_D	7.05	7.06
	C_L	0.530	0.532
15 deg	C_L/C_D	3.94	3.88
	C_L	0.920	0.954

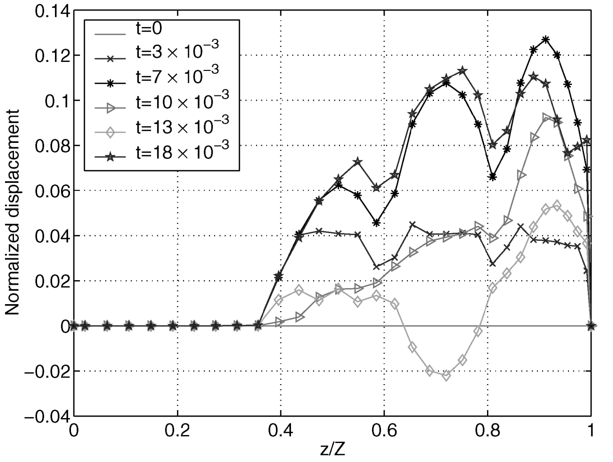

Fig. 10 Time history of trailing-edge displacement for membrane wing at α = 6 deg. The camber at the root is 0.90 cm.

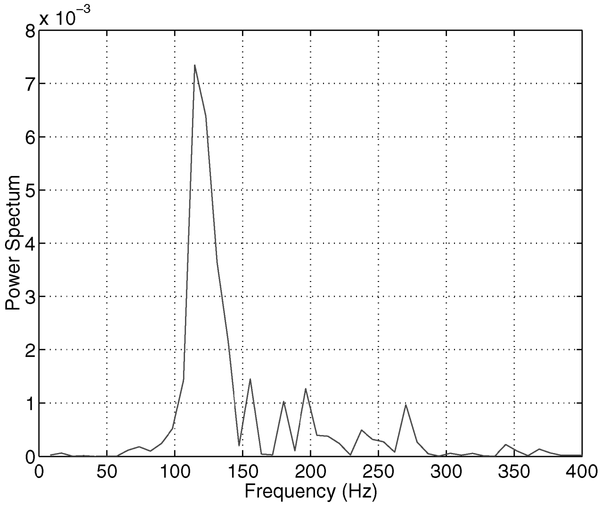

Fig. 11 Spectrum analysis of the trailing-edge point vibration for membrane wing at α = 6 deg.

points also show dominated frequencies around 120 Hz, which is comparable to the experimental frequency of 140 Hz (Ref. 3). The experimental conditions and the detailed wing configuration between the present case and those reported by Waszak et al.[3] are not identical. Hence, the qualitative agreement between computation and experiment in this regard is deemed satisfactory. Liu[25] has reported that, under a typical wing gust situation, the energy is mainly located in the low-frequency range of several hertz or lower. This membrane fluctuates in a timescale much faster than either the vehicle control scale or the expected wing gust timescale; hence, the membrane fluctuation is not expected to cause sensitive response to the vehicle.

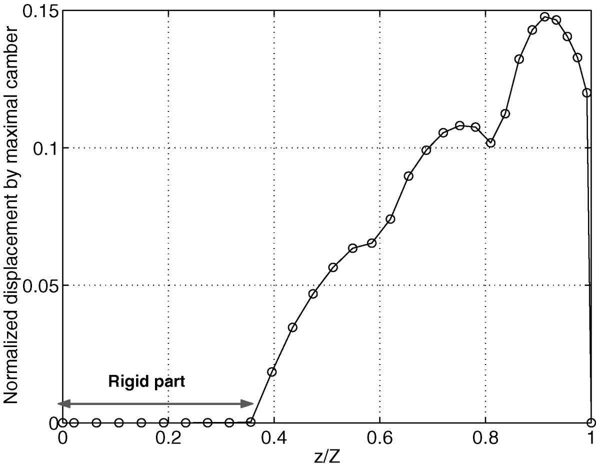

a) α = 6 deg

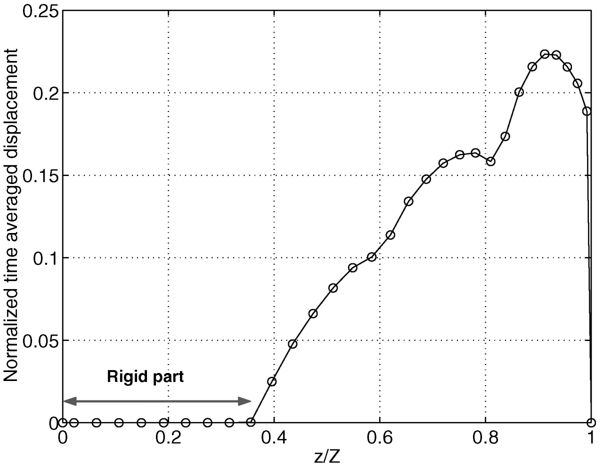

b) α =15 deg

Fig. 12 Averaged displacement of the membrane-wing trailing edge.

With the same freestream condition, as shown in Table 2, the flexible wing exhibits slightly less lift coefficient than the rigid one at $\alpha = 6$ deg. The difference in the C_L/C_D is also small. At a higher angle of attack of 15 deg, the membrane wing generates a lift coefficient about 2% less than that of the rigid wing; however, its C_L/C_D is 1.5% larger than that of the rigid one. These differences lie behind the high-frequency membrane vibration. Under the external force, the membrane wing changes its shape. This shape change has two effects. On the one side, it decreases the lift by reducing the effective angle of attack of the membrane wing; on the other side, it increases the lift by increasing the camber. The present finding that membrane and rigid wings exhibit comparable aerodynamic performance before stall limit is also experimentally observed by Waszak et al.[3]

Figure 12 shows the time-averaged vertical displacement of the membrane wing trailing edge. This displacement is also normalized by the maximal camber of the wing. On average, the maximal displacement occurs near the tip. At $\alpha = 6$ deg, it is about 15% of the camber, and it increases to approximately 22% at $\alpha = 15$ deg. The kinks shown in the figure correspond to the batten locations. Because of this movement, the effective angle of attack of the membrane wing is less than the rigid one. We compare their spanwise angles of attack in Fig. 13. In Fig. 13a, the rigid wing has an incidence of 6 deg at the root and monotonically increases to 9.5 deg at the tip; the membrane wing shares the same angles of attack with the rigid wing within 36% of the inner wing largely because of the rigidity of the root; however, in the outer side, its effective angle of attack is less than that of the rigid wing. At the tip, the effective angle of attack of the membrane wing is smaller than that of the rigid one by about 0.8 deg Fig. 13b compares the angle of attack at $\alpha = 15$ deg, the effective angle of attack of the membrane wing is more than 1 deg smaller than that of the rigid one at the tip. This reduced effective angle of attack causes the decrease in the lift.

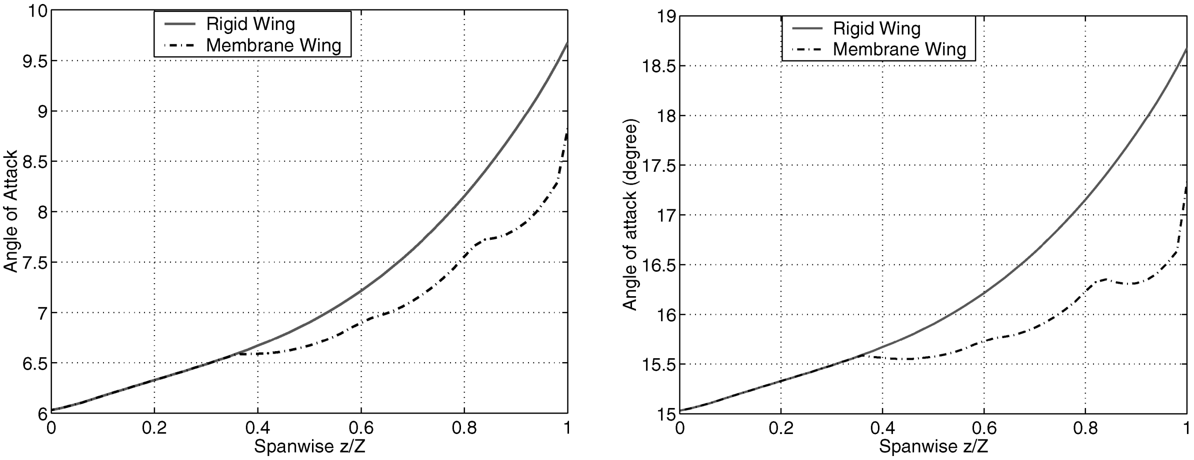

a) α = 6 deg

b) α =15 deg

Fig. 13 Averaged angle of attack for membrane wing.

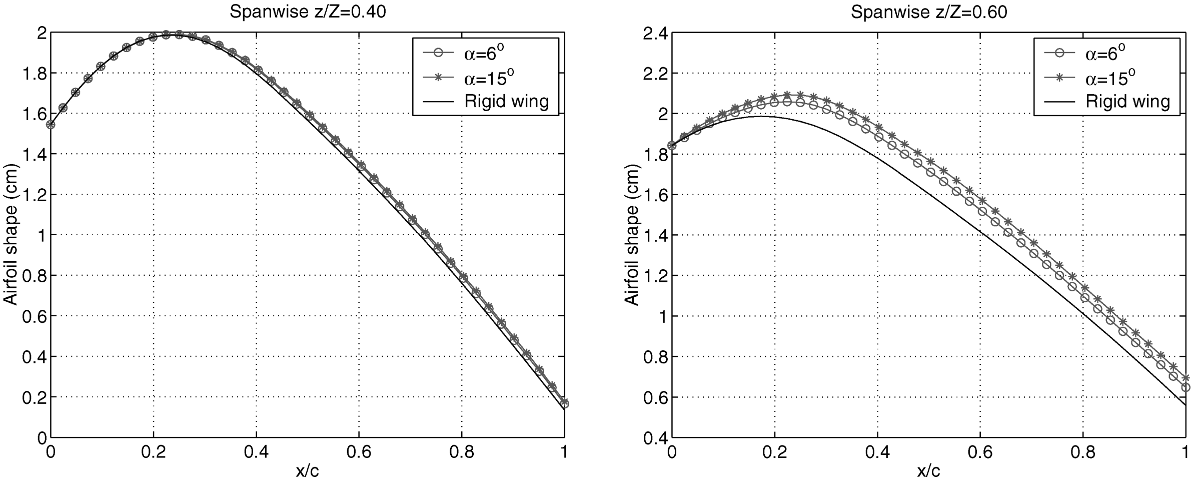

a) Numerical results at *x*/*c* = 0.4

b) Numerical results at *x*/*c* = 0.6

Fig. 14 Averaged spanwise airfoil shape for membrane wing with experimental results at *x*/*c* = 0.5 (Ref. 3).

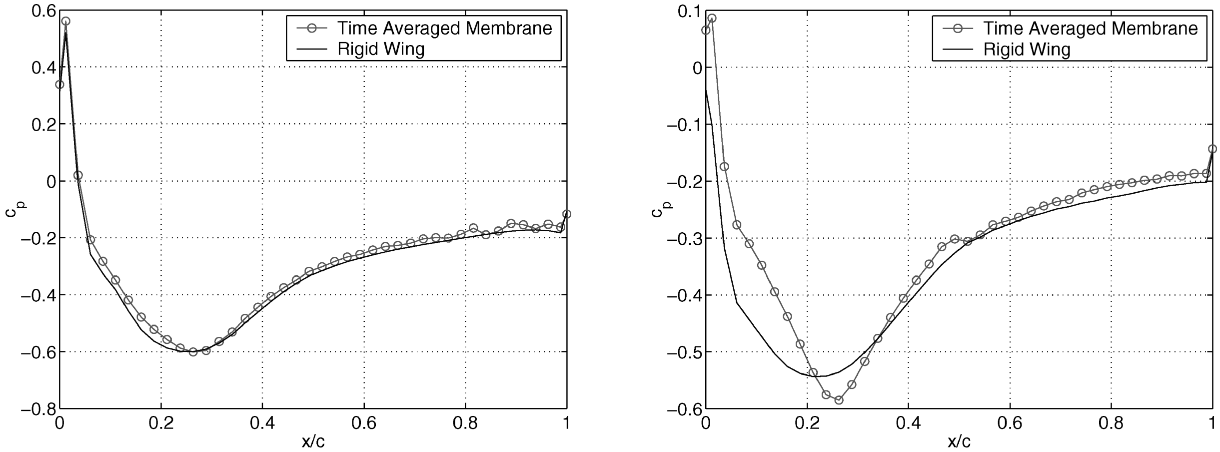

a) *x*/*c* = 0.4

b) *x*/*c* = 0.6

Fig. 15 Chordwise c_p comparison at two different spanwise locations between time averaged membrane wing and steady rigid wing at α = 6 deg.

The shape change of the membrane wing has another effect; it increases the wing camber. The increased camber is shown in Fig. 14. Two airfoil shapes at different spanwise positions are plotted together with the corresponding rigid-wing shape. The camber increase is more visible in the outer wing than in the inner wing. This is consistent with Fig. 12, where the maximal trailing-edge displacement occurs near the tip. As expected, the increase is larger at $\alpha = 15$ deg than that at $\alpha = 6$ deg. Figure 14c shows the experimental results by Waszak et al.[3] Because the bending stiffness of the batten is not considered in our computations, the displacement at the trailing edge is smaller than that of the experimental results. The movement of the wing surface affects the overall pressure distribution. In the spanwise direction, as shown in Fig. 15, the pressure difference between the membrane and rigid wings is smaller at inboard where the displacement is smaller and is larger at outboard where the displacement is relatively larger.

IV. Summary

The aerodynamic performance of a membrane wing is investigated numerically. To accurately simulate the interaction between the flexible membrane structure and its surrounding viscous flow, a coupled fluid and structure computation is performed. Time synchronization between the fluid solver and structure solver significantly reduces the error caused by phase lag. The geometric conservation law is important in moving boundary problems. Without satisfying it, the computation shows irregular spikes in the C_L/C_D. Such spikes disappear after the law is enforced. For comparative purpose, the rigid-wing dynamics is also investigated. Based on the solutions obtained, we make the following observations:

1) Tip vortices play an important role in the low-aspect-ratio wing. They reduce the effective angle while bringing low-pressure regions that provide additional lift.

2) The low-Reynolds-number flow on the upper wing surface is prone to separate because of the adverse pressure gradient. The separation first occurs near the root section because of the larger camber there.

3) Tip vortices and separated flow cause unsteady phenomenon on the wing. However, the aerodynamic coefficient differences between the steady and unsteady computations are small for the nominal range of angles of attack considered here.

4) The membrane wing vibrates even in a steady freestream. Both computational and experimental studies indicate that under steady-state freestream the membrane vibrates with $\mathcal{O}(10^2)$ Hz.

5) Typically, the membrane wing maintains lower effective angle of attack than the rigid wing of the same baseline configuration because of the trailing edge moves up under the external forces. However, the shape inflation causes the membrane wing exhibit a larger camber than the rigid, which increases the lift. Overall, the member wing and the rigid wing has comparable lift at modest angles of attack.

6)Before reaching the stall limit, the time-averaged membrane wing behaviors, including lift and drag, seem to be consistent with that of the rigid wing. These observations are also reported by Waszak et al.[3] in their experimental investigation.

In the future, the effect of high angle of attack and the implications of unsteady freestream will be reported.

Acknowledgment

The present work has been supported by the U.S. Air Force. We have benefited from interaction with Dr. Ifju and his students.

References

[1] Shyy, W., Berg, M., and Ljungqvist, D., “Flapping and Flexible Wings for Biological and Micro Vehicles,” *Process in Aerospace Sciences*, Vol. 35, No. 5, 1999, pp. 455–506.

[2] Lian, Y., Shyy, W., Viieru, D., and Zhang, B. N., “Membrane Wing Aerodynamics for Micro Air Vehicles,” *Process in Aerospace Sciences*, Vol. 39, 2003, pp. 425–465.

[3] Waszak, R. M., Jenkins, N. L., and Ifju, P., “Stability and Control Properties of an Aeroelastic Fixed Wing Micro Aerial Vehicle,” AIAA Paper 2001-4005, 2001.

[4] Lian, Y., Shyy, W., Ifju, P., and Verron, E., “Membrane Model for MAVs,” *AIAA Journal*, Vol. 41, 2003, pp. 2492–2494; also AIAA Paper 2002-2972, 2002.

[5] Jackson, P. S., and Christie, G. W., “Numerical Analysis of Three-Dimensional Elastic Membrane Wings,” *AIAA Journal*, Vol. 25, 1987, pp. 676–682.

[6] Smith, R. W., and Shyy, W., “Computational Model of Flexible Membrane Wings in Steady Laminar Flow,”*AIAA Journal*, Vol. 33, 1995, pp. 1769–1777.

[7] Shyy, W., Udaykumar, H. S., Rao, M. M., and Smith, R. W., *Computational Fluid Dynamics with Moving Boundaries*, Taylor and Francis, Washington, DC, 1996.

[8] Shyy, W., *Computational Modeling for Fluid Flow and Interfacial Transport*, Elsevier, Amsterdam, 1994.

[9] Thomas, P. D., and Lombard, C. K., “Geometric Conservation Law and Its Application to Flow Computations on Moving Grids,” *AIAA Journal*, Vol. 17, 1979, pp. 1030–1037.

[10] Lian, Y., “Membrane and Adaptively-Shaped Wings for Micro Air Vehicles,” Ph.D Dissertation, Dept. of Mechanical and Aerospace Engineering, Univ. of Florida, Gainesville, FL, 2003.

[11] Duchon, J. P., “Splines Minimizing Rotation-Invariant Semi-Norms in Sobolev Spaces,” *Constructive Theory of Functions of Several Variables*, edited by W. Schempp, and K. Zeller, Springer-Verlag, Berlin, 1977, pp. 85–100.

[12] Mooney, M., “A Theory of Large Elastic Deformation,” *Journal of Applied Physics*, Vol. 11, 1940, pp. 582–592.

[13] Wilson, E. L., Farhoomand, I., and Bathe, K. J., “Nonlinear Dynamic Analysis of Complex Structures,” *Earthquake Engineering and Structural Dynamics*, Vol. 1, 1973, pp. 241–252.

[14] Issa, R. I., “Solution of the Implicitly Discretised Fluid Flow Equations by Operator-Splitting,” *Journal of Computational Physics*, Vol. 62, 1985, pp. 40–65.

[15] Reuther, J., Alonso, J. J., Rimlinger, M. J., and Jameson, A., “Aerodynamic Shape Optimization of Supersonic Aircraft Configuration via an Adjoint Formulation on Distributed Memory Parallel Computers,”*Computers and Fluids*, Vol. 28, 1999, pp. 675–700.

[16] Lian, Y., Steen, J., Trygg-Wilander, M., and Shyy, W., “Low Reynolds Number Turbulent Flows around a Dynamically Shaped Airfoil,” *Computers and Fluids*, Vol. 32, 2003, pp. 287–303.

[17] Ifju, P., Jenkins, D., Ettinger, S., Lian, Y., Shyy, W., and Waszak, R. M., “Flexible-Wing-Based Micro Air Vehicles,” AIAA Paper 2002-0705, Jan. 2002.

[18] Anderson, J. D., Jr., *Introduction to Flight*, 3rd ed. McGraw–Hill, New York, 1989.

[19] Mueller, T. J., and Delaurier, J. D., “ Aerodynamics of Small Vehicles,” *Annual Review of Fluid Mechanics*, Vol. 35, 2003, pp. 89–111.

[20] Young, A. D., and Horton, H. P., “Some Results of Investigation of Separation Bubbles,” AGARD, Vol. 4, 1966, pp. 779–811.

[21] Crompton, M. J., and Barrett, R. V., “Investigation of the Separation Bubble Formed Behind the Sharp Leading Edge of a Flat Plate at Incidence,” *Journal of Aerospace Engineering*, Vol. 214, 2000, pp. 157–176.

[22] Cummings, R. M., Morton, S. A., Siegel, S. G., and Bosscher, S., “Numerical Prediction and Wind Tunnel Experiment for a Pitching Unmanned Combat Air Vehicle,” AIAA Paper 2003-0417, Jan. 2003.

[23] Gordnier, R. E., and Visbal, M. R., “Development of a Three-Dimensional Viscous Aeroelastic Solver for Nonlinear Panel Flutter,” *Journal of Fluids and Structures*, Vol. 16, 2002, pp. 497–527.

[24] Farhat, C., Geuzaine, P., and Grandmont, C., “The Discrete Geometric Conservation Law and the Nonlinear Stability of ALE Schemes for the Solution of Flow Problems on Moving Grids, ” *Journal of Computational Physics*, Vol. 174, 2001, pp. 669–694.

[25] Liu, H. T., “Unsteady Aerodynamics of a Wortmann Wing at Low Reynolds Number,” *Journal of Aircraft*, Vol. 29, 1992, pp. 532–539.